The Interaction of Tides with the Sill of a Tidally Energetic Inlet

MICHAEL W. STACEY

Institute of Ocean Sciences, Sidney, B.C. V8L 4B2, Canada

ABSTRACT

The interaction of the tides with the sill of a tidally energetic inlet, Observatory Inlet, British Columbia, is studied. Because of temporal variations in the stratification of the inlet, a substantial seasonal variation is observed in the power withdrawn from the barotropic tide. Vigorous, nonlinear, internal motions occur in the region of the sill, but most of the withdrawn tidal power is fed into a progressive, linear internal tide. The first two modes, which contain almost all of the energy, respond very differently to changes in stratification. The energy flux of the first mode is insensitive to changes in surface stratification but increases dramatically as a result of deep water renewal. The energy flux of the second mode exhibits the reverse behavior, being insensitive to the occurrence of deep water renewal but being a strong positive function of the surface stratification. Even though the inlet has a distinct surface layer in summer and appears to be a two-layer system, the second mode contains almost as much power as the first, a characteristic not indicative of simple two-layer flows.

The nonlinear sill processes induce a significant baroclinic flow at the beat frequency of the M_2 and S_2 tides. This flow is most vigorous near the surface of the inlet where it is greater in magnitude than the M_2 barotropic current.

1. Introduction

This paper is an examination of the interaction of the barotropic tide with the sill of a deep, stratified, tidally energetic inlet. In particular, Observatory and Portland Inlets, located on the coast of British Columbia, are studied.

There are a number of recognized ways in which the tides can influence the circulation of an inlet. Farmer and Smith (1979) found that the tidal currents in the vicinity of the sill of Knight Inlet cause the occurrence of many interesting phenomena (flow separation, hydraulic jumps, bores, finite-amplitude lee waves) and that the type of flow observed is a function of the stratification and the tidal velocity. They classified the observed flows in terms of internal Froude numbers, $F_n = \bar{u}/c_n$, where $\bar{u}$ is the maximum barotropic tidal velocity over the sill and c_n is the phase speed according to linear theory of the nth internal mode over the sill. Freeland and Farmer (1980) found that the power withdrawn from the barotropic tide in Knight Inlet was similarly correlated to the stratification, increasing in the summer when the stratification increased and then decreasing as winter approached. One might speculate, therefore, that much of the power withdrawn from the barotropic tide goes into the nonlinear processes occurring at the sill. There are other routes, however, by which the energy can leave the surface tide.

Energy may also be fed into linear, progressive, internal waves such as those described by Stigebrandt (1976, 1980). Stigebrandt used a simple linear model to estimate the energy flux of progressive, internal waves generated by the interaction of the tides with the sill of an inlet. Stigebrandt (1979) finds evidence for such waves in Oslofjord.

Power is always lost from the barotropic tide by frictional drag against the boundaries of the inlet. However, the percentage of the total power withdrawn from the barotropic tide in this manner in a deep inlet will normally be quite small. Freeland and Farmer (1980) estimate that in Knight Inlet frictional drag accounts for no more than about 3% of the power withdrawn from the barotropic tide. Also, this mechanism cannot explain the seasonal variation observed by Freeland and Farmer in the power withdrawn from the barotropic tide.

Even though most of the energy withdrawn from the barotropic tide is eventually dissipated, mixing will cause an increase in the potential energy of the inlet if the water column is stratified. If most of the power withdrawn from the barotropic tide goes into the sill processes, observed by Farmer and Smith (1979), most of the increase in potential energy will take place in the vicinity of the sill. Frictional processes can also cause significant mixing over the sill if the sill is both long, relative to a tidal excursion, and shallow. The horizontal pressure gradients which result from such mixing may initiate density currents at the sill such as those described by Drinkwater and Osborn (1975). If most of the energy withdrawn from the barotropic tide goes into the progressive, internal waves described

by Stigebrandt (1976, 1980), mixing will take place where the internal waves break (if they are not reflected) at the boundaries of the inlet. Stigebrandt also reasons that this mixing causes the formation of density currents at the boundaries, and that these density currents then cause further mixing by flowing into the interior of the inlet.

Observatory and Portland Inlets (Fig. 1) offer an opportunity to estimate the influence of a number of these processes on the circulation of a tidally energetic inlet. This paper focuses mainly on the role of the internal tide in modulating the currents of the inlet. It is found that, even though nonlinear processes occur in the region of the sill, a linear model very similar to that used by Stigebrandt (1976, 1980) will account for much of the divergence of the observed tidal current from purely barotropic flow. Also, the power withdrawn from the barotropic tide is adequately predicted by the linear model. Nonlinear processes have a significant influence on the flow, however, particularly near the surface of the inlet where they induce a baroclinic current at the beat frequency of the M_2 and S_2 semidiurnal tides.

2. The inlet system and the data

Observatory Inlet is a fjord located just south of the Alaska Panhandle on the coast of British Columbia (Fig. 1). The sill of Observatory Inlet is located about 50 km from the open ocean and has a maximum depth of about 60 m. The inlet itself is $\sim$2.5 km wide within 30 km of the sill and reaches a maximum depth of $\sim$500 m. About 30 km landward of the sill the inlet widens rather abruptly and $\sim$40 km from the sill branches into two parts, Alice Arm and Hastings Arm.

The inlet seaward of the sill, Portland Inlet, is about twice as wide as Observatory Inlet and deepens uniformly towards the open ocean. Branching off the northern boundary of Portland Inlet is the Portland Canal which itself is connected to the Pearse Canal. Work Channel and Khutzeymateen Inlet branch off the southern boundary of Portland Inlet.

In December 1981 anemometers, tide gages, thermistor chains and current meters were deployed by the Institute of Ocean Sciences (IOS) in the configuration shown in Fig. 1. They were maintained until April 1983. The details of the deployment are described below and tabulated in Table 1.

Two tide gages each were deployed at Salmon Cove, Lizard Cove, and Pearson Point. All were AMS model 750A except for one Aanderaa 3A at Pearson Point.

The current-meter mooring at OBS1 had an Aanderaa RCM-4 at 10 m and a Neil Brown at 50 m. The mooring at OBS2 had RCM-4s at 10, 50 and 100 m. The mooring at OBS3 was designed to have RCM-4s at 10, 40, and 100 m, but, because the mooring site was located near a trough, small variations in the mooring position at times resulted in significant depth .
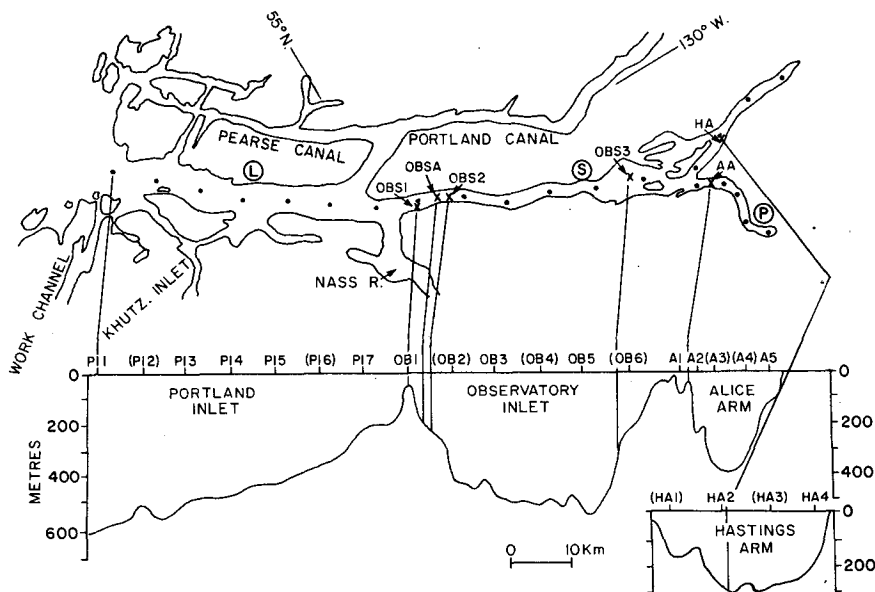

FIG. 1. Plan view and longitudinal section of the inlet system. Tide gages are located at Lizard Cove ⓛ, Salmon Cove ⓢ and Pearson Point ⓟ. Current meter moorings are located at OBS1, OBS2, OBS3 and AA. Anemometers are located at OBSA and HA. Thermistor chains are located at OBSA, OBS3 and AA. CTD stations are indicated by the solid circles in the plan view and by alphanumeric symbols in the longitudinal section. The alphanumeric symbols in parentheses indicate locations where oxygen measurements were made on a regular basis. Mooring OBS1 was located near the middle of the channel. It is displaced in the figure so that the CTD station can be shown.

TABLE 1. The instruments that were deployed at the locations shown in Fig. 1.

Location	Current meter depths (m)	Thermistor chain depths (m)	Number of anemometers	Number of tide gages
OBS1	10, 50			
OBSA		(1) 5 to 55	1	
		(2) 60 to 110		
OBS2	10, 50, 100			
OBS3†	10, 40, 100	(1) 12.5 to 37.5		
		(2) 45 to 95		
AA	10, 40	(1) 12.5 to 37.5		
HA			1	
Lizard Cove				2
Salmon Cove				2
Pearson Point				2

† See the text for comments on variations that occurred in the depth of deployment.

changes. The current meters were periodically deployed about 60 m deeper than intended. The mooring at AA had RCM-4s at 10 and 40 m.

The mooring at OBS3 had two thermistor chains. One was doubled and extended from 12.5 to 37.5 m (when the mooring was properly deployed) with 2.5 m separating each thermistor. The other extended from 45 to 95 m (when the mooring was properly deployed) with 5 m separating each thermistor. The mooring at AA had a doubled thermistor chain extending from 12.5 to 37.5 m. The anemometer mooring at OBSA had two thermistor chains, one extending from 5 to 55 m, the other extending from 60 to 110 m. There was another anemometer in Hastings Arm.

When the moorings were being serviced (once every two or three months) CTD casts and oxygen samples were taken at regular intervals along Portland and Observatory Inlets (Fig. 1).

Generally, the data return was good, except between June and September 1982 when current data from only AA were recovered. Also, the anemometer at OBSA malfunctioned during the winter of 1983. This paper primarily utilizes current data from OBS2, the tide data from Lizard Cove and Salmon Cove and the CTD data close to the sill.

The major source of freshwater runoff into Portland and Observatory Inlets is the Nass River which flows into Portland Inlet about 5 km from the sill. Fig. 2a shows the monthly discharges of freshwater from the Nass River for the year 1982. The maximum discharge in June is caused primarily by meltwater. The CTD stations taken in Portland and Observatory Inlets indicate that freshwater from the Nass River penetrated about 30 km up-inlet during the summer of 1982, and that near the sill the freshwater layer was approximately 10 m deep. In winter the density varied almost linearly

from top to bottom. Fig. 3 shows representative sigma-t profiles for summer and winter.

The CTD profiles (Fig. 4), in conjunction with the oxygen measurements (Fig. 5), reveal that deep water renewal of Observatory Inlet occurred between June and September 1982. Unfortunately, between June and September there are current data only from mooring AA. The sigma-t contours in Fig. 4 show that between June and September the density of Observatory Inlet below sill depth increased significantly. Figure 5a shows that down-inlet of the sill the oxygen concentrations below sill depth decreased significantly between June and September. Fig. 5b shows that up-inlet of the sill the oxygen concentrations below sill depth also for the most part decreased. The oxygen concentrations up-inlet of the sill in September are similar to oxygen concentrations down-inlet of the sill in June.

The tides in Portland and Observatory Inlets, to be described in more detail later, are dominated by the semidiurnal M_2 (12.42 h) component which has an amplitude of about 1.9 m. During spring tides the tidal velocity over the sill can exceed 1 m s^{-1}. The tidally forced nonlinear sill processes observed in Knight Inlet by Farmer and Smith (1979) are also observed by acoustic methods to significantly influence the circulation near the sill in Observatory Inlet (Farmer and Freeland, 1983). It is shown below that the effect of these processes on the circulation of the inlet is clearly evident in the current data. It is also shown, however, that linear processes have an even more important influence on the baroclinic flow.

3. Power removed from the barotropic tide

The energy to produce much of the baroclinic flow in a tidally energetic inlet comes from the barotropic
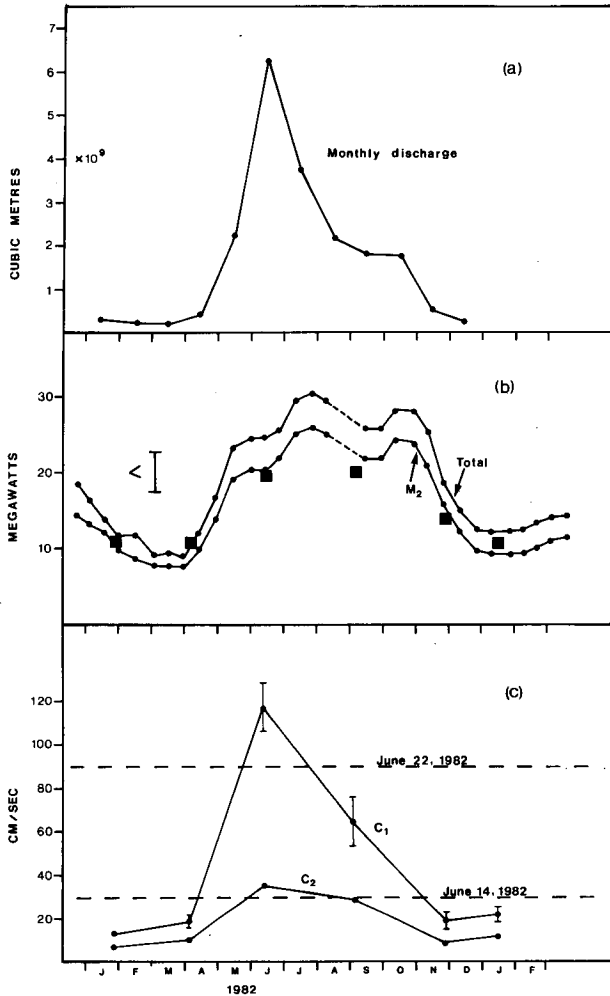
FIG. 2. (a) Monthly freshwater runoff from the Nass River for the year 1982. (b) Power removed from the barotropic tide. The upper curve is the power removed from the five most important tidal components. The lower curve is the power removed from the M_2 tide alone. The solid squares indicate the energy flux of the M_2 internal tide as predicted by the linear model described in the text. (c) Phase speeds over the sill of the first two internal wave modes. The horizontal straight lines indicate the maximum sectionally averaged tidal velocities over the sill for a typical spring and neap tide.

tide, so it is of great interest to know the rate at which energy is being removed from the barotropic tide. A method very similar to that used by Freeland and Farmer (1980) is used here to calculate the rate at which the energy is removed.

The net flux of tidal energy across any section of an inlet of arbitrary shape is given by

$$P = \int\!\!\int_{\text{Area}} \rho g \overline{u\eta} ds, \qquad (1)$$

where the overbar indicates an average over a tidal cycle, ρ is the water density, g the acceleration due to gravity, and u and η are the barotropic tidal velocity and height at the section of interest (Garrett, 1975).

The double integral represents integration over the section area. The tidal height between Lizard and Salmon Coves varies by less than 5%, so, following Freeland and Farmer (1980), a given component of the tidal height between Lizard and Salmon Coves can be approximated as $\eta = \eta_0 \sin(\omega t)$, where η_0 is the amplitude of the tidal height and ω is its angular frequency. The velocity of the tidal component at a given section of the inlet can be expressed as $u = u_0 \cos(\omega t - \epsilon)$ where u_0 is the amplitude of the velocity at the section and ϵ is the phase shift caused by the removal upstream of the section of energy from the barotropic tide. By invoking continuity one finds, if ϵ is small, that $u_0 \approx (\eta_0 \omega S)/A$, where S is the surface area of the inlet upstream of the section and A is the cross-sectional area of the section. Therefore, one finds from (1) that the power removed from the tidal component upstream of the section of interest is

$$P \approx \rho g \frac{\eta_0{}^2 \omega S}{2} \sin(\epsilon). \qquad (2)$$

In an inlet of constant width (2) reduces to the expression used by Freeland and Farmer (1980). In Portland and Observatory Inlets the inlet width varies significantly, so the assumption of constant width cannot be made.

Before one can calculate the power removed from the barotropic tide the phase shift ϵ must be determined. Freeland and Farmer (1980) show how this can be accomplished from measurements of the tidal height. The formulation presented here is a generalization of their technique. Suppose there are two tide gages in an inlet and that they are located at sections 1 and 2 as shown in Fig. 6. The height and velocity indicated at section 2 in Fig. 6 differ from those of Freeland and Farmer in that they are not assumed to be in quadrature. Freeland and Farmer assumed that $\phi_1 = \phi_2$, i.e., that "all of the energy lost by a tidal wave is lost between sections 1 and 2". It is shown below that this is not a necessary assumption. Following Freeland and Farmer, one has

$$A_1 u_1 \cos(\omega t - \epsilon) - A_2 u_2 \cos(\omega t - \phi_2)$$

$$\approx S_0 \frac{d}{dt}\left[\frac{h_1 \sin(\omega t) + h_2 \sin(\omega t - \phi_1)}{2}\right] \qquad (3)$$

from which, if ϵ, ϕ_1 and ϕ_2 are small, we obtain

$$\epsilon \approx \left[1 - \frac{S_0}{2S_1}\right]\phi_1 + \frac{A_2 u_2}{A_1 u_1}(\phi_2 - \phi_1)$$

$$= \left[1 - \frac{S_0}{2S_1}\right]\phi_1 + \frac{S_2}{S_1}(\phi_2 - \phi_1), \qquad (4)$$

where A_i ($i = 1, 2$) is the cross-sectional area of section i, and S_i ($i = 1, 2$) is the surface area of the inlet upstream of section i; S_0 is the surface area between the two sections.
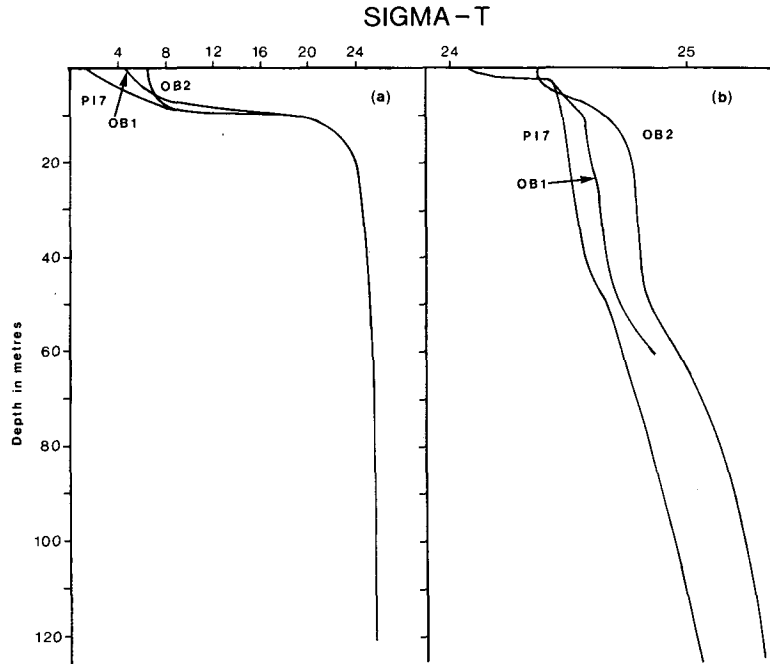
SIGMA - T

FIG. 3. Typical sigma-t profiles near the sill during (a) summer (12 June 1982), and (b) winter (28 January 1982). Note that the abscissas in (a) and (b) are scaled differently.

Letting P be equal to the total power removed from the barotropic tide upstream of section 1, we have from (2) that

$$P \approx \frac{\rho g \eta_0^2 \omega S_1}{2} \sin(\epsilon) \tag{5}$$

which, if ϵ is small, becomes

$$P \approx \frac{\rho g \eta_0^2 \omega S_1}{2}\left[1 - \frac{S_0}{2S_1}\right]\phi_1 + \frac{\rho g \eta_0^2 \omega S_2}{2}(\phi_2 - \phi_1). \tag{6}$$

Since the second term on the rhs of (6) is obviously equal to the power removed from the barotropic tide upstream of section 2, the first term on the rhs is the

power removed from the barotropic tide between sections 1 and 2. In an inlet of constant width this term reduces to the expression used by Freeland and Farmer (1980). One now sees that it remains an admissible expression for the power lost between sections 1 and 2 even when the power lost upstream of section 2 is significant.

The tide gages at Lizard Cove and Salmon Cove were used to calculate η_0 and ϕ_1 for the principal tidal components. Twenty-nine day data blocks were Fourier transformed after first removing the mean and trend, and successive data blocks were chosen to overlap by 14.5 days. The drift in the clocks of each instrument was taken into account when calculating the phase of the tidal components.
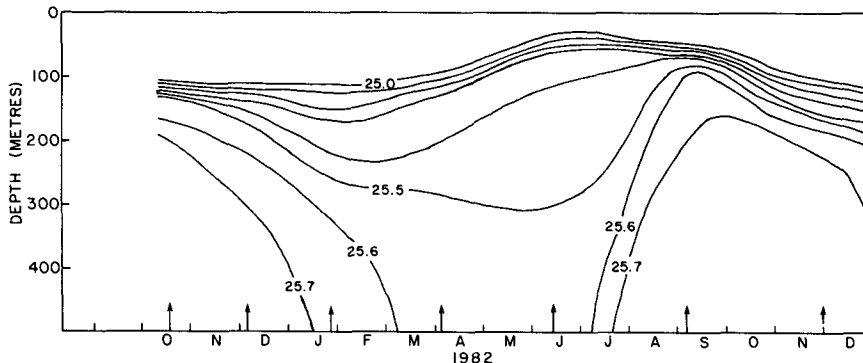

FIG. 4. Sigma-t contours at OB4. The arrows on the abscissa indicate when CTD profiles were taken. No contours shallower than the $\sigma_t = 25$ contour are shown.
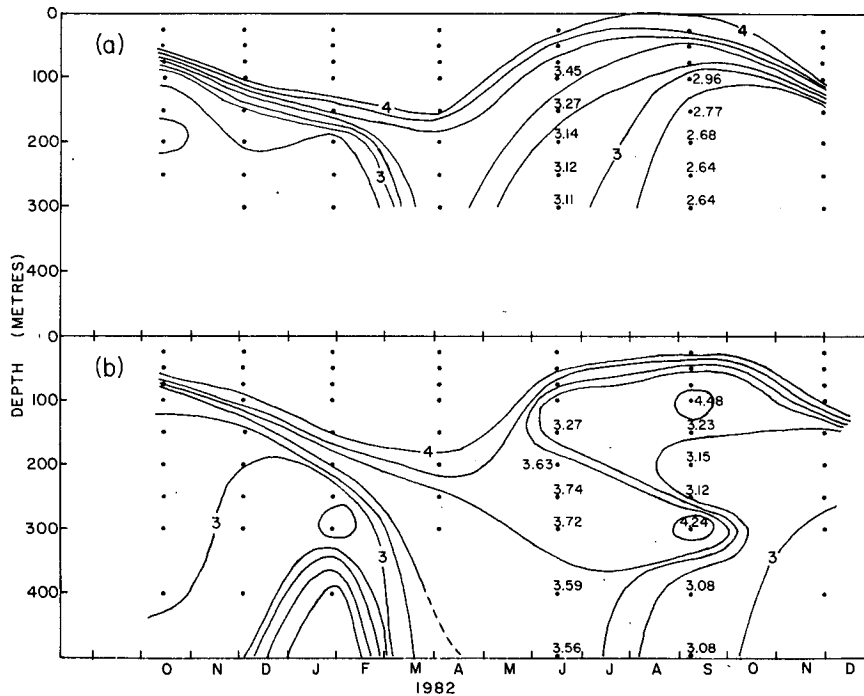
FIG. 5. Dissolved oxygen (ml l⁻¹) at (a) PI6 and (b) OB4. No contours shallower than the 4 ml l⁻¹ contour are shown.

The power removed from five tidal components, M_2, $S_2 + K_2$, N_2, $K_1 + P_1$ and O_1, was calculated. The sum of these power losses, and the power lost by the M_2 component alone are plotted in Fig. 2b. We observe that the M_2 tide accounts for almost all of the power loss. The calculated amplitude of the M_2 tide remained relatively constant from data block to data block at 1.9 to 2 m. The amplitude of the next most important tidal component, the S_2 tide, varied from 0.46 to 0.85 m, however, and the remaining tidal components exhibited similar variations in amplitude. This is perhaps not surprising in light of the somewhat short length of each data block and the dominance of the M_2 signal in the tidal record. The error bars were determined by estimating the rms noise level in the tidal spectra between the diurnal and semidiurnal bands, and then calculating the average error that a random vector of this magnitude ($\sim$7 mm) would give
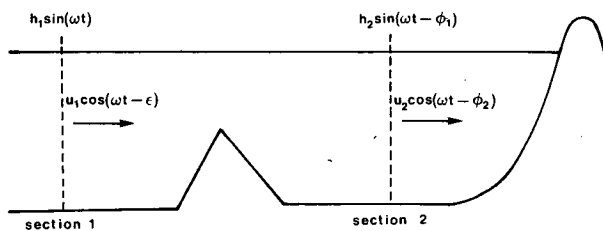

FIG. 6. Diagram of the inlet system showing the tidal velocity and height at two sections of the inlet. Lizard Cove corresponds to section 1 and Salmon Cove corresponds to section 2.

to the M_2 tidal component. Freeland and Farmer (1980) show that the average error is $N/(\sqrt{2}A)$, where N and A are the amplitude of the noise and the M_2 tidal component respectively. They also note that the errors determined in this way are probably too large, possibly because of "cusping around the diurnal and semidiurnal bands."

One sees that the increase in freshwater runoff in June is correlated to an increase in P. The small increase in P in July is likely in response to the occurrence of deep water renewal (Figs. 4 and 5). The small increase in P in October may correspond to a secondary peak in freshwater input caused by increased precipitation in the autumn, but, in general, the decrease in P lags the decline in freshwater input.

There is an obvious seasonal dependence in P that cannot be explained by bottom friction. Also, even the magnitude of P is much greater than can be accounted for by bottom friction. Using

$$P = \rho\kappa \int\int_{\text{Area}} |\vec{u}|^3 ds, \qquad (7)$$

where the double integral indicates integration over the surface area of the inlet between Lizard and Salmon Coves, and κ, a drag coefficient, is equal to 0.003 (see Freeland and Farmer, 1980), it is estimated that bottom friction can account for no more than about 0.2 megawatt of the power withdrawn from the barotropic M_2 tide. Clearly, other processes must account for the

majority of the power being withdrawn from the barotropic tide.

4. Sill processes

Farmer and Smith (1979) found that the nonlinear sill processes in Knight Inlet increase in intensity with increasing surface stratification, and can be successfully classified in terms of appropriately defined Froude numbers. The power withdrawn from the barotropic tide in Knight Inlet is similarly correlated to the stratification (Freeland and Farmer, 1980), which leads one, as mentioned in the Introduction, to speculate that most of the power goes into these nonlinear processes. Froude numbers like those of Farmer and Smith (see below) can also be calculated for Observatory Inlet. Although the Froude numbers cannot by themselves be used to examine quantitatively the energetics of sill processes, they can be used to estimate how closely correlated these processes are to the power being withdrawn from the barotropic tide. The higher the correlation the more likely it is that a significant portion of the power withdrawn from the barotropic tide does indeed go into the sill processes.

Farmer and Smith defined their Froude numbers as $F_n = \bar{u}/c_n$ where c_n is the phase speed of the nth internal mode with M_2 frequency and $\bar{u}$ is the maximum sectionally averaged tidal velocity over the sill. The phase speeds are determined from the solution to the eigenvalue problem

$$\left. \begin{array}{c} \dfrac{d^2 \hat{W}_n(z)}{dz^2} + \left(\dfrac{N^2}{\omega^2} - 1 \right) k_n^2 \hat{W}_n(z) = 0 \\[12pt] \hat{W}_n(0) = \hat{W}_n(H) = 0 \end{array} \right\} \quad , \quad (8)$$

where $W_n(x, z, t) = \hat{W}_n(z) \exp[i(k_n x \pm \omega t)]$ is the vertical velocity of the nth mode, k_n its wavenumber, N the Brunt-Väisälä frequency (determined from CTD profiles) and H is the depth of the bottom boundary. Rotation is neglected in this problem because the sill processes respond only weakly to the rotation. In analogy with the procedure of Farmer and Smith, the bottom boundary is chosen to be sill depth (maximum depth $\sim$ 60 m for Observatory Inlet) because upstream blocking and flow separation occur, and "the behavior of the flow over the crest will depend principally upon the density structure down to sill depth." Fig. 2c shows the phase speeds as a function of time of the first two modes. Each phase speed is the average of those speeds calculated from the three CTD stations closest to the sill. If CTD stations were taken both when the ship was steaming into and out of the inlet then the speed is the average of six individual values. The error bars on the mode-one speeds are standard deviations. The maximum sectionally averaged tidal velocities over the sill for a typical spring and neap tide are also drawn in Fig. 2c.

We see immediately that the mode-one Froude

number in particular is better correlated to freshwater runoff than to the amount of power being withdrawn from the barotropic tide. This implies that the barotropic tide is supplying significant amounts of energy to other internal processes. The fact that the deep water renewal between June and September seems to cause a noticeable increase in the power removed from the barotropic tide (see Figs. 2b, 4 and 5) implies that at least some of the power goes into motions much deeper than sill depth. Likely candidates for these deeper motions are the progressive internal waves proposed by Stigebrandt (1976, 1980).

5. The internal tide

The linear model presented here is a slight generalization of Stigebrandt's (1976, 1980) model. Following Stigebrandt, the sill is approximated as an infinitely thin strip, and the bottom near the sill is assumed to be flat. Contrary to Stigebrandt, the depths of the inlet on opposite sides of the sill are allowed to differ. Fig. 7 shows the simplified topography used to represent Portland and Observatory Inlets. The walls of the inlets are assumed to be vertical. There is perhaps some doubt about the suitability of the flat-bottom assumption on the seaward side of the sill because there the bottom, over most of its length, deepens continuously away from the sill. However, near the sill, where the bottom is almost flat, the assumption should be valid. On the landward side of the sill the depth of the inlet ($\sim$400 m) is taken to be the most representative depth.

The barotropic velocity of a single tidal component just seaward of the sill is expressible as

$$u_b(x, t) = \frac{S(x)\omega}{A_b} \eta_0 \cos(\omega t), \qquad (9)$$

where A_b is the cross-sectional area of the inlet just seaward of the sill and $S(x)$ is the surface area of the inlet upstream of the position x. The barotropic tidal velocity over the sill is

$$u_s(t) = \frac{S(0)\omega}{A_s} \eta_0 \cos(\omega t) = U_s \cos(\omega t), \qquad (10)$$
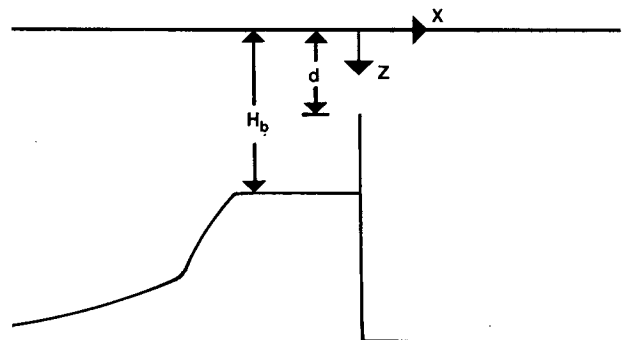

FIG. 7. Simplified topography used to model the tidal motion near the sill.

where A_s is the cross-sectional area over the sill. There must, of course, be no volume flux through the sill. This boundary condition at the sill can be satisfied by superimposing the barotropic tidal velocity given by (9) with progressive internal waves for which the velocities take the form $u_n = a_n \hat{u}_n(z) \cos(\omega t + k_n x)$. The constant a_n is determined from the boundary condition at the sill. The velocity field becomes

$$u(x, z, t) = \frac{S(x)}{A_b} \omega \eta_0 \cos(\omega t)$$

$$+ \sum_{n=1}^{\infty} a_n \hat{u}_n(z) \cos(\omega t + k_n x), \quad (11)$$

where

$$\frac{S(0)}{A_b} \omega \eta_0 + \sum_{n=1}^{\infty} a_n \hat{u}_n(z) = \begin{cases} U_s, & 0 \leqslant z < d \\ 0, & d \leqslant z \leqslant H_b, \end{cases} \quad (12)$$

is the boundary condition at the sill, d is the depth of the sill (average depth $\sim$50 m), and H_b is the depth of the inlet just seaward of the sill ($\sim$200 m). By continuity

$$\hat{u}_n(z) = \frac{1}{k_n} \frac{d\hat{W}_n}{dz}, \quad (13)$$

where $\hat{W}_n(z)$ is a solution to (8) with $H = H_b$. From (12) and (13) one finds that

$$a_n = \frac{-U_s \hat{W}_n(d) k_n}{\int_0^{H_b} [d\hat{W}_n/dz]^2 dz}. \quad (14)$$

The energy transport away from the sill of the nth internal mode is

$$\epsilon_n = W E_n c_{g,n}, \quad (15)$$

where W is the width of the inlet near the sill ($\sim$2.5 km), E_n the energy density of the nth mode, and $c_{g,n}$ the group velocity of the nth mode. In shallow water the group velocity is, of course, equal to the phase speed c_n. The energy density of the nth mode is

$$E_n = \rho \int_0^{H_b} \overline{u_n^2} dz = \frac{\rho}{2} \int_0^{H_b} a_n^2 \hat{u}_n^2 dz \quad (16)$$

from which we obtain

$$\epsilon_n = \frac{\rho W c_n U_s^2 \hat{W}_n^2(d)}{2 \int_0^{H_b} [d\hat{W}_n/dz]^2 dz}. \quad (17)$$

The total rate of energy transport away from the seaward side of the sill is

$$\epsilon_T = \sum_{n=1}^{\infty} \epsilon_n. \quad (18)$$

It is justifiable to neglect rotation in this calculation because, by assumption, internal plane waves are generated at the sill. As these waves progress away from the sill they will adjust to the rotation of the earth by becoming Kelvin waves but this adjustment will not cause their energy flux to change.

The energy transport away from the landward side of the sill is calculated in the same way. The total depth is now the depth of the inlet landward of the sill and the velocities of the progressive internal waves take the form $a_n \hat{u}_n(z) \cos(\omega t - k_n x)$. Also, it is now assumed that the internal waves are completely absorbed upon encountering the boundaries of the inlet, so that there are no reflected waves to influence the flow near the sill. This assumption is in line with the view of Stigebrandt (1976) who proposes that breaking internal waves at the boundaries of inlets are a source of energy for mixing. One does not need to make this assumption on the seaward side of the sill because the internal waves generated there do not encounter boundaries that would tend to reflect them back towards the sill. It is shown later that the measured differences in phase between the isopycnals and the along-channel baroclinic current velocity are consistent with the existence up-inlet of the sill of progressive internal waves.

The total energy flux away from the sill is the sum of the fluxes on both sides of the sill, and it can be calculated numerically from the available CTD data. More precisely, the density data from the CTD station at PI7 (see Fig. 1) is used to solve the eigenvalue problem (8) for the values of c_n and $\hat{W}_n(z)$ down-inlet of the sill, and the CTD station at OB2 is used to solve for the values of c_n and $\hat{W}_n(z)$ up-inlet of the sill. Substitution of c_n and $\hat{W}_n(z)$ into (17) allows the energy flux away from the sill of the nth mode to be determined and (18) gives the energy flux due to all the modes. Because the CTD profiles were taken every two or three months, one can calculate the energy flux of the internal tide as a function of time. The predicted total fluxes caused by power withdrawn from the M_2 barotropic tide, summed over the first ten modes, are plotted in Fig. 2b. They are very similar to the values that have been calculated from the phase shifts in the measured M_2 tidal height. To check the sensitivity of the model predictions to the depth of the bottom boundary on the seaward side of the sill (recall that there the bottom over much of its length deepens continuously away from the sill) the energy flux was also calculated using density data from station PI6 instead of PI7. This allowed the bottom boundary on the seaward side of the sill to be set at a depth of about 300 m instead of 200 m. The largest percentage increase in the predicted total energy flux resulting from this change occurs in April 1982 when the total flux increases by 2.2 megawatts or about 20%. The basic conclusion, namely that the predicted energy flux of the internal waves is similar to the power removed from the M_2 barotropic tide, is unaltered. This strongly implies that the rate

at which energy is withdrawn from the barotropic tide is controlled by the rate at which energy can be put into the internal tide.

Figure 8 shows the energy flux as a function of time of the first three internal modes. The successive modes ($n = 4, 5, 6, \ldots$) are no more important to the total flux than the third mode. The first two modes are responsible for at least 90% of the predicted total energy flux (except in January 1983 when they account for 88% of the total flux), and the division of power between them can vary substantially with time. The model implies that the increase in power withdrawn from the M_2 barotropic tide in June is caused primarily by an increase in the energy flux of the mode-two internal wave. By September, when the fresh surface layer has become much less distinct, flux of the mode-one wave has increased and flux of the mode-two wave has decreased leaving the total flux almost unchanged. The temporal dependence of the mode-two flux is qualitatively similar to the temporal dependences of

the freshwater runoff and Froude numbers shown in Fig. 2. This suggests that the mode-two flux is sensitive to the amount of freshwater input. The mode-one energy flux responds very weakly to the sudden June increase in freshwater runoff, but the increased mode-one flux in September suggests that it has been significantly influenced by the occurrence of deep water renewal. The stratification obviously has an important influence on the energy fluxes associated with each mode. The importance of the mode-two internal wave in June suggests that, even though the water column in summer appears to be composed of two distinct layers (Fig. 3a), a two-layer model would not give an adequate representation of the tidally forced circulation in the inlet.

The phase speeds associated with the first and second modes are also plotted in Fig. 8. Stigebrandt (1980) has suggested that the validity of the above model for the case of constant N is doubtful if the Froude number constructed from the mode-one phase speed and the
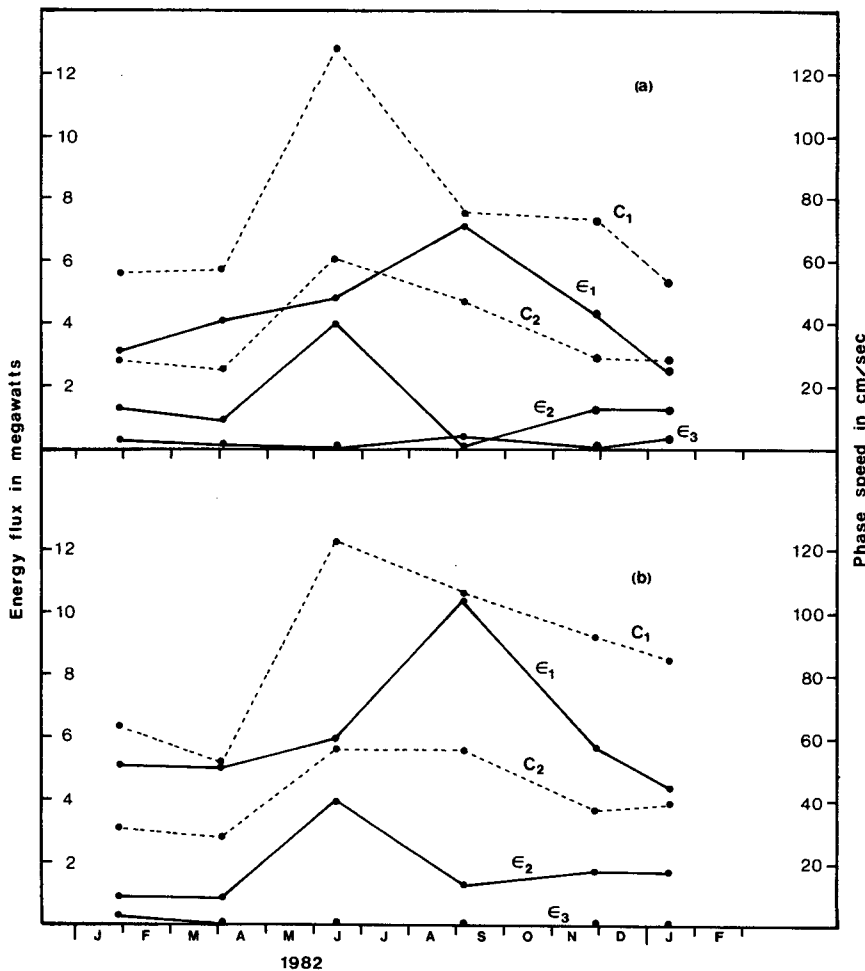

FIG. 8. Energy fluxes of the first three modes and phase speeds of the first two modes in (a) Portland Inlet and (b) Observatory Inlet.

maximum barotropic tidal velocity over the sill is greater than about one, i.e., if

$$F_1 = \frac{U_s}{c_1} > 1.$$

From the definition of U_s [see (10)] one finds that $U_s \approx 50$ cm s^{-1} for the M$_2$ tide. Therefore, on both sides of the sill U_s is always less than the mode-one phase speed. This means that the flow is indeed always subcritical according to Stigebrandt's definition of the Froude number, which is perhaps why the model accurately predicts the rate of energy removal from the barotropic tide. At times the Froude number is almost equal to one which implies that nonlinearities are becoming important, but even then the model adequately predicts the amount of power being removed from the barotropic tide. This Froude number differs from that of Farmer and Smith (1979) because they use the maximum sectionally averaged tidal velocity due to superposition of all tidal components, and calculate the phase speed from (8) using a different value for H. They take the bottom boundary to be at sill depth, whereas here the bottom boundary is taken to be the bottom of the inlet. According to Farmer and Smith's definition of the mode-one Froude number the flow is often supercritical and, even when the flow is subcritical, nonlinear sill processes are observed to occur. It appears, not surprisingly, that more than one Froude number is required to classify the flow. Stigebrandt's definition may adequately parameterize the range of validity of the linear model, but Farmer and Smith's definition probably provides a better classification of nonlinear processes in the region of a sill.

Stratification also has a significant effect on the energy density of each mode. In Fig. 9 the ratio of the predicted energy densities of the first two modes is
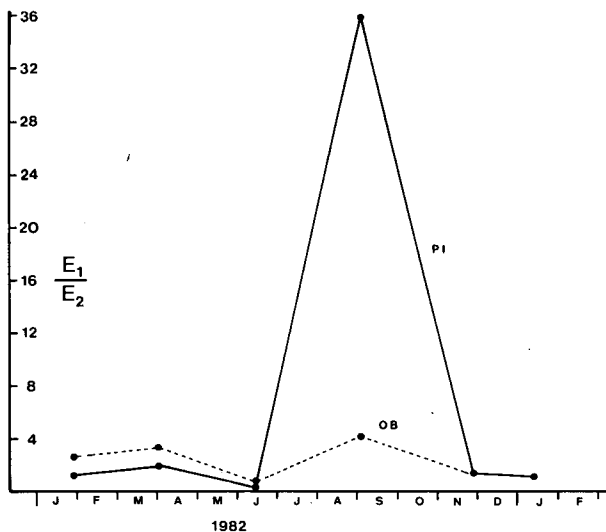

FIG. 9. Ratio of the energy densities of the first two modes.

plotted against time. In Observatory Inlet the ratio changes by about a factor of six between June and September. In Portland Inlet it changes by about a factor of one hundred. Stigebrandt (1980) has shown that, for the case of constant N, the ratio of the sill depth to the total depth has an important influence on the relative amount of energy contained in each mode. Here, one sees that the amount of energy contained in each mode is also a very strong function of the stratification itself. It is perhaps worth noting in particular that, although the fresh surface layer in summer is only a small percentage of the total volume of the inlet, the second mode is very sensitive to the surface stratification. Therefore, it may be that omission of the thin surface layer in theoretical studies of inlets will, at times, result in inaccurate predictions even when the phenomenon being studied occurs far from the surface.

6. Observations of the internal tide

The current data from OBS2 and the tidal data from Salmon Cove can be used to determine the baroclinic current velocity at OBS2 for comparison with the theoretical predictions of the linear model. The current meter site is only ~3.5 km from the sill in 220 m of water, so the bottom boundary was set at 200 m (instead of 400 m) when doing the theoretical calculations. Also, the density profiles at OB2 were used in the theoretical calculations.

The linear model presented in this paper neglects the influence of rotation, but one can estimate the error in the predicted velocity that results from this simplification. The plane waves generated at the sill must respond to the rotation of the earth by developing a cross-channel slope that varies as $\exp(-y/R_n)$, where R_n is the Rossby radius of deformation of the nth mode, i.e., $R_n = c_n/f$ where f is the Coriolis parameter. The velocity of propagation of the waves c_n is unaltered by the rotation of the earth (Gill, 1982, p. 379). So, in order for the energy flux of the Kelvin waves to be the same as that of the plane waves from which they evolved, one must have [see (15) and (16)]

$$\int_0^{H_b} \int_0^W a_n{}^2 \hat{u}_n{}^2 dy dz$$

$$= \int_0^{H_b} \int_0^W (b_n \exp(-y/R_n))^2 \hat{u}_n{}^2 dy dz$$

or

$$\frac{b_n}{a_n} = \left\{ \frac{2W}{R_n} [1 - \exp(-2W/R_n)]^{-1} \right\}^{1/2}, \quad (19)$$

where $b_n \exp(-y/R_n)$ is a measure of the cross-channel variation in amplitude of the mode-n Kelvin wave. At the position $y = W/2$ (the middle of the channel and the approximate position of the current meter site) the

ratio of the amplitude of the velocity of the Kelvin wave to that of the plane wave is

$$K_n = \frac{b_n}{a_n} \exp\left(-\frac{W}{2R_n}\right).$$

The factor K_n differs most from unity in the winter. In January 1982 $R_1 \approx 4$ km and $K_1 \approx 0.97$; $R_2 \approx 2$ km and $K_2 \approx 0.88$. In June 1982, on the other hand, $R_1 \approx 10$ km and $K_1 \approx 1.0$; $R_2 \approx 4$ km and $K_2 \approx 0.97$. These differences between the plane-wave and Kelvin-wave solutions are felt to be acceptably small. The differences are even smaller than this if the waves have not yet fully adjusted to the rotation of the earth by the time they reach the current meter site.

Figure 10 shows theoretical profiles, due to superposition of the first ten internal modes, of the along-channel M_2 baroclinic current for January 1982. They correspond to distances from the sill of 2, 4 and 6 km. The phase profiles in Fig. 10b are the amount by which the barotropic current leads the baroclinic current. At the sill the barotropic and baroclinic currents are in phase.

Two 29-day data blocks of the tides and the along-channel current velocities, one beginning 1900 GMT 26 December 1981 and the other beginning 2230 GMT 26 January 1982 were Fourier transformed. The first data block covers the month before the January CTD

FIG. 10. Amplitude (a) and phase (b) of the M_2 baroclinic current velocity. The January 1982 CTD data at OB2 were used in the theoretical calculation. The symbols ⊛ and ★ designate the measured amplitudes and phases at OBS2 that were calculated from data blocks of the currents and tides beginning 26 December 1981 and 26 January 1982 respectively.

profile was taken, and the second data block covers the month after the profile was taken. The tide data yield the barotropic M_2 component of the current velocity. The current data yield the total M_2 component of the current velocity. The baroclinic current velocity is obtained from the total velocity after the barotropic component, calculated from the tides, has been removed. The amplitudes and phases of this baroclinic current are plotted in Fig. 10. The amplitude at OBS2 of the barotropic current velocity is 8 cm s^{-1}, so the baroclinic velocities of 10–20 cm s^{-1} are relatively very important.

The theoretical profiles in Fig. 10 representing the distance 4 km from the sill correspond most closely to the location of the current meter site. At 4 km from the sill the theoretical amplitude agrees well with the measured amplitude at the depths of 50 and 100 m, but overestimates the amplitude at the depth of 10 m. Given that 1) the amplitude along the inlet varies significantly at all depths (according to the theory), 2) the inlet is not exactly flat as assumed by the model and 3) possible nonlinear effects are not being taken into account, the agreement between the theory and the measurements is quite good.

The theoretical phase 4 km from the sill is larger than the measured phase at 10 and 50 m, and smaller than the measured phase at 100 m. Again, the sensitivity of the phase to the along-inlet position, and the assumption of a flat bottom and linear flow probably account for much of the discrepancy. The measured phase (the difference in phase between the barotropic and baroclinic velocities) is significant and strongly suggests the existence of an internal tide.

Figure 11 shows theoretical profiles of the M_2 baroclinic current for September 1982, a period when more power was being withdrawn from the barotropic tide than during January 1982. No current data between June and September 1982 exist for OBS2 so only one 29-day data block, beginning 2330 GMT 31 August 1982 has been Fourier transformed. The measured amplitudes and phases are plotted in Fig. 11. Although the model overestimates the amplitude of the velocity at a depth of 10 m, the predicted amplitudes are in very good agreement with the measured amplitudes at 50 and 100 m. The phase at 10 and 50 m is also well predicted. The discrepancy between the predicted and observed phases at 100 m is most likely caused by the overestimation of the amplitude at 10 m. To satisfy continuity the predicted current must reverse at a shallower depth than the observed current.

Time series of sigma-t data exist for each current meter so that, as a further check on the validity of the linear model, the difference in phase between the M_2 components of the baroclinic velocity and the isopycnals can be estimated. The sigma-t data corresponding to the January 1982 and September 1982 data blocks mentioned above were Fourier transformed. Table 2 shows the predicted and observed differences in phase
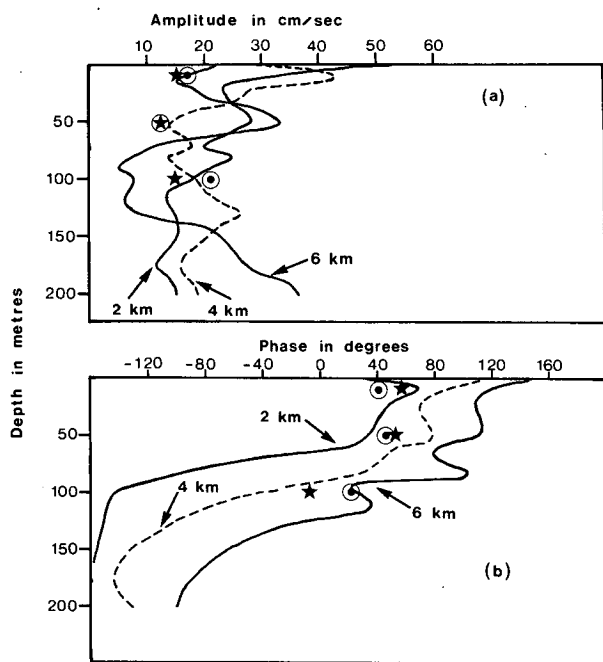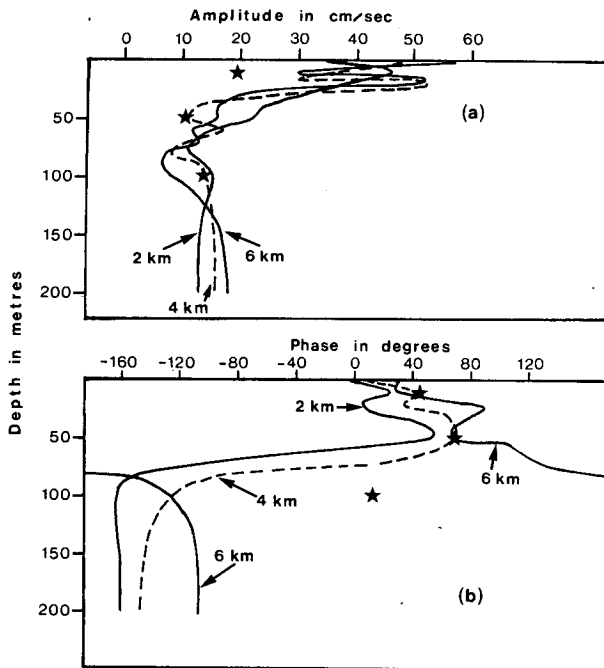
FIG. 11. Amplitude (a) and phase (b) of the M_2 baroclinic current velocity. The September 1982 CTD data at OB2 were used in the theoretical calculation. The symbol ★ designates the measured amplitudes and phases at OBS2 that were calculated from data blocks of the current and tides beginning 31 August 1982.

between the velocity and the isopycnals. The predicted phase of the isopycnals is found simply by integrating the predicted vertical velocity with respect to time. The theory agrees well with the measurements at 10 and 50 m. In September the predicted and observed phases at a depth of 100 m differ substantially, but, this is not surprising since the linear model poorly predicts the phase of the baroclinic velocity at 100 m also (see Fig. 11b). In general, these measurements provide support for the existence of a progressive internal tide.

Farmer and Smith's Froude number (Fig. 2c) and the predicted energy flux in the mode-two internal wave (Fig. 8) are largest in June, so it would have been nice to have been able to test the predictive ability of the linear model then. Presumably, the nonlinear sill processes were most vigorous in June. Unfortunately, the data return from the current meters in June was not good. Only the current meter at 100 m returned data (in May and early June) that can be used to test the theory. Fourier transforming twenty-nine day data blocks of the tides and currents, beginning 1530 GMT 11 May 1982, an M_2 baroclinic current with an amplitude of 13 cm s^{-1} was obtained. It lagged the barotropic M_2 current by -7 deg. The predicted amplitude 4 km from the sill at at a depth of 100 m is 10 cm s^{-1} and the predicted phase lag is -74 deg. One sees, therefore, that even in June the amplitude of the current at 100 m is well predicted. At the current meter site

the nonlinear sill processes evidently have little influence on the amplitude of the M_2 baroclinic flow below sill depth.

7. Nonlinear processes

Freeland and Farmer (1980) noted that the sill processes in Knight Inlet are more vigorous during spring tides than during neap tides, presumably because more energy is available for mixing during springs. This causes the baroclinic current to be modulated at the beat frequency of the M_2 and S_2 tides, i.e., the MSf frequency which has a period of 14.7 days. A significant MSf signal has also been observed in Observatory Inlet (Farmer and Freeland, 1983). This means that, although the baroclinic flow in Observatory Inlet is dominated by the M_2 internal tide, the nonlinear processes occurring at the sill significantly influence the circulation also.

To examine this more closely a 73.5-day data block of currents and tides, beginning 1930 GMT 18 January 1983, has been Fourier transformed. This data length was chosen so that the MSf, M_2 and S_2 frequencies would be Fourier frequencies. The amplitudes and phases of the M_2, S_2 and MSf current velocities are tabulated in Table 3. One sees that the MSf baroclinic current is much larger than the MSf barotropic current, and at a depth of 10 m is even larger than the M_2 barotropic current. At 50 m (approximately sill depth) the MSf baroclinic current is substantially smaller than the M_2 and S_2 currents, but at 100 m it is as large as the S_2 baroclinic current. Note also that the phase of the MSf baroclinic current changes by about 180 deg between 10 and 100 m. It seems reasonable, based on this information, to speculate that the MSf baroclinic current is mode one with the node near sill depth.

In addition to the MSf signal, the current record at 10 m has a number of much higher frequency peaks corresponding to periods of about 6 h. These peaks have amplitudes of about 2 cm s^{-1}, and occur at frequencies that are sums and differences of the M_2, S_2 and MSf frequencies.

It is evident from the current record that nonlinear interactions noticeably influence the circulation, particularly at the depth of 10 m. This is precisely where

TABLE 2. Predicted and observed differences in phase between the M_2 components of the isopycnal variation and the baroclinic current velocity. The phases given are the amount in degrees by which the current velocity lags the isopycnal variation.

Depth (m)	January 1982		September 1982	
	Predicted	Observed	Predicted	Observed
10	135	156	221	227
50	170	157	199	194
100	88	109	35	126

TABLE 3. Amplitudes and phases of the M_2, S_2 and MSf current velocities.

	M_2		S_2		MSf	
	Amplitude (cm s^{-1})	Phase (deg)	Amplitude (cm s^{-1})	Phase (deg)	Amplitude (cm s^{-1})	Phase (deg)
Barotropic	8.0	63.6	3.3	358.0	0.007	150.8
Baroclinic at 10 m	14.7	112.6	6.3	64.5	11.8	313.2
Baroclinic at 50 m	13.3	98.3	6.1	49.8	1.8	261.9
Baroclinic at 100 m	14.8	97.6	5.2	30.3	5.7	136.3

the linear model overestimates the amplitude of the M_2 baroclinic current (Figs. 10 and 11). If the model is indeed an accurate description of linear flow in the inlet this suggests that possibly nonlinear interactions are transferring energy from M_2 to MSf and other frequencies.

8. Summary and conclusions

The interaction of the barotropic tide with the sill of Observatory Inlet has been examined. The power withdrawn from the barotropic tide, due to the interaction of the tide with the sill of the inlet, exhibits a strong temporal dependence that frictional processes alone cannot explain. A simple theoretical model shows that most of the power is being fed into progressive linear internal waves with M_2 frequency. The baroclinic currents associated with these internal waves are clearly evident in the available current data, and they are stronger than the barotropic component of the M_2 tidal current. The first two internal wave modes account for almost all of the energy removed from the barotropic tide, and the partitioning of energy between them is a very strong function of the manner in which the water column is stratified. The predicted energy flux of the mode-one wave was insensitive to the summer increase in surface stratification, but increased dramatically as a result of the occurrence of deep water renewal. The predicted energy flux of the mode-two wave increased with the summer increase in surface stratification but was insensitive to the occurrence of deep water renewal. In summer, when there was a distinct surface layer, the predicted energy flux of the mode-two wave was almost as large as that of the mode-one wave. This implies that a simple two-layer model of the inlet would not have given an accurate description of the flow. By September, after the decline in surface stratification and the occurrence of deep water renewal, the predicted energy flux of the mode-two wave had become almost negligible relative to that of the mode-one wave.

Nonlinear processes are also clearly evident in the current record. The beating of the M_2 and S_2 tides results in a significant baroclinic MSf current which, near the surface of the inlet, is stronger than the M_2 barotropic current. However, at the current meter site and presumably even farther from the sill, these nonlinear processes have less influence on the baroclinic flow than the internal tide.

REFERENCES

Drinkwater, K. F., and T. R. Osborn, 1975: The role of tidal mixing in Rupert and Holberg Inlets, Vancouver Island. *Limnol. Oceanogr.*, **20**, 518–529.

Farmer, D. M., and J. D. Smith, 1979: Tidal interaction of stratified flow with sill in Knight Inlet. *Deep-Sea Res.*, **27A**, 239–254.

——, and H. J. Freeland, 1983: The physical oceanography of fjords. *Progress in Oceanography*, Vol. 12, Pergamon, 147–220.

Freeland, H. J., and D. M. Farmer, 1980: Circulation and energetics of a deep, strongly stratified inlet. *Can. J. Fish. Aquat. Sci.*, **37**, 1398–1410.

Garrett, C. J. R., 1975: Tides in gulfs. *Deep-Sea Res.*, **22**, 23–36.

Gill, A. E., 1982: *Atmosphere-Ocean Dynamics*, Academic Press, 662 pp.

Stigebrandt, A., 1976: Vertical diffusion driven by internal waves in a sill fjord. *J. Phys. Oceanogr.*, **6**, 486–495.

——, 1979: Observational evidence for vertical diffusion driven by internal waves of tidal origin in the Oslofjord. *J. Phys. Oceanogr.*, **9**, 435–441.

——, 1980: Some aspects of tidal interaction with fjord constrictions. *Estuarine Coastal Mar. Sci.*, **11**, 151–166.